# Single-Atom Fe-N$_4$ sites promote the triplet-energy transfer process of g-C$_3$N$_4$ for the photooxidation

Junhui Wang [*], Shimin Yin, Qinhua Zhang, Fengliang Cao, Yicheng Xing, Qingshan Zhao, Yang Wang, Wengang Xu, Wenting Wu [*], Mingbo Wu

*State Key Laboratory of Heavy Oil Processing, College of Chemical Engineering, Institute of New Energy, China University of Petroleum (East China), Qingdao 266580, PR China*

**ABSTRACT**

Polymeric carbon nitride materials show intriguing prospects in numerous light-to-energy conversion applications, but seldom studies focus on their triplet energy transfer, leading to the insufficient lifetime for the photochemical process. Inspired by the porphyrin molecular photocatalyst, single-atom sites (Fe-N$_4$) as triplet sensitizing sites were fabricated in g-C$_3$N$_4$ for the preparation of Fe-g-C$_3$N$_4$, which processes a long-lived triplet emissive state ($\tau_{PH}$ = 4.93 μs). But under realistic condition for the large-scale production of catalyst, single atoms are inevitable to sinter, resulting in the formation of other metal species. Therefore, the photooxidation of 1,5-dihydroxynaphthalene (1,5-DHN) and the photocatalytic E-Z Isomerization of stilbene were selected as the model reactions to evaluate the influence of various Fe species on the triplet energy transfer. It was found that Fe-N$_4$ sites promote the triplet energy transfer process, while Fe nanoclusters (Fe$^0$) promote the electron transfer and inhibit triplet energy transfer. This finding provides guidance for the rational design of photocatalysts to efficiently improve triplet energy transfer process and its application.

© 2021 Elsevier Inc. All rights reserved.

## 1. Introduction

Polymeric carbon nitride materials, as versatile and reliable heterogeneous photocatalysts, show intriguing prospects in water splitting [1–5], CO$_2$ reduction [6,7], and recent synthesis of the value-added organic compounds [8–13]. The overwhelming majority of arguments focus on photogenerated electron regulation for the improvement of photocatalytic performances [13–16].Whereas the energy transfer, especially for the long-lived triplet energy transfer process and its relationship with electron transfer, have seldom been explored. Actually, triplet excitons can afford unique electron distribution and enough lifetime for the rich photochemical and photophysical process.

Intersystem crossing process (ISC) is an essential step for the triplet energy transfer, and it strongly needs the assistant of triplet sensitizing sites, which have been deeply studied in numerous molecular photocatalysts such as heavy atom site [17–20] (e.g. Pt (II), Ir(III) and Ru(II) complexes, Iodine complex), transition metal-nitrogen coordination sites (M−N$_4$, e.g. M = Fe, Zn, Ni) in porphyrin [21,22] and aromatic ketone site [23] et al. Although molecular photocatalyst is expensive and difficult reuse, its exact triplet sensitizing site provides inspiration for the fabrication of heterogeneous photocatalysts.

Similar to molecular photocatalysts, single-atom photocatalysts (SACs), in which isolated metal atoms are atomically located on the suitable supports, provide the ideal strategy to create highly efficient catalysts at molecular level [24–26]. For polymeric carbon nitride, it processes rich nitrogen source and provides abundant N coordination site for metal ions, which is beneficial for the formation of M−N$_x$ triplet sensitizing site [27]. Under realistic reaction condition for the large-scale SACs production, there is a significant challenge, that is single atoms are inevitable to shift and easy sinter, resulting in a few other metal species (e.g. Fe$^0$) in SACs. The nature of metal sites responsible for the triplet energy transfer activity in M−N$_x$ SACs still remains elusive to date.

Herein, the model photocatalyst with single-atom Fe-N$_4$ site embedded in g-C$_3$N$_4$ (Fe-g-C$_3$N$_4$) was designed and prepared through one-step pyrolysis of FeCl$_3$ and dicyandiamide, which provides an economic method for heterogeneous triplet photocatalyst. Other metal species in photocatalysts were finely tuned through the ratio of FeCl$_3$ and dicyandiamide under the same pyrolysis temperature. In terms of singlet oxygen ($^1$O$_2$) generally generated through triplet energy transfer, it is one of the most important reactive oxygen species (ROS) with the promise in the selective organic synthesis [28–30]. Associated with the quenching, acid

---

bleaching and optical tests, the photocatalytic oxidation of 1,5-dihydroxynaphthalene (1,5-DHN) were used to evaluate the influence of metal species on the triplet energy transfer ability and its competing relationship with the electron transfer. The E-Z isomerization reaction of stilbene (higher triplet energy level than $^1O_2$) provides further proof for the universality of the photosensitizer. This work would provide guidance for the rational design of heterogeneous photocatalysts with triplet state properties and their applications.

## 2. Materials and methods

### 2.1. Materials

Dicyandiamide and anhydrous ferric chloride were purchased from Shanghai Aladdin Biochemical Technology Co., Ltd. 1,5-Dihydroxynaphthalene (98%) was purchased from Sinopharm Chem. Reagent Co. (Beijing, China). All reagents were used without further purification.

### 2.2. Synthesis of $C_3N_4$ and Fe-g-$C_3N_4$

g-$C_3N_4$ and Fe-g-$C_3N_4$ single-atom photocatalysts were prepared by calcining precursors (only dicyandiamide for g-$C_3N_4$, mixture of $FeCl_3$ and dicyandiamide for Fe-g-$C_3N_4$) at 550 ℃ with a ramp rate of 2 ℃ min$^{-1}$ for 4 h under $N_2$ flow (for more details, see the Supporting Information).

### 2.3. Density functional theory calculations

To study the structure of Fe single atom site embedded in g-$C_3N_4$, theoretical studies were performed by DFT calculations. On the basis of experimental analysis, possible models of g-$C_3N_4$, FeTPP and Fe-g-$C_3N_4$-10 are established by use of Gaussian09. The ground-state geometries of the models were optimized by DFT methods with B3LYP/3-21G basis set.

### 2.4. Photocatalytic of $^1O_2$ generation test

15.0 mg of photocatalyst was added to a 50 mL round-bottom flask containing 20 mL of acetonitrile/water = 5:1 mixed solution, and stirred to make it evenly dispersed. 200 μL of 1,5-DHN (c = 1 × $10^{-2}$ M) was added into the add round-bottom flask. After stirring for 30 min under dark conditions to achieve adsorption–desorption equilibrium, the reaction solution was irradiated with an LED lamp (white light) with a power of 10 W and a light intensity of 120 W·m$^{-2}$ and stirred continuously. Samples were taken every 15 min for testing. The substrate can be clearly observed through the ultraviolet–visible spectrum (1,5-DHN) the absorption peak at 300 nm gradually decreases, and the absorption peak of the product (juglone) at 425 nm continuously increases.

The yield of juglone was calculated using following equation:

$$Yield = \frac{100 \times A_{i(Juglone)} / \varepsilon_{(Juglone)}}{C_{initial(1,5-DHN)}} \times 100\%$$

$A_{i(Juglone)}$ represents the ultraviolet absorbance of juglone;
$\varepsilon_{(Juglone)}$ represents the molar extinction coefficient of juglone ($\varepsilon$ = 3567 M$^{-1}$cm$^{-1}$);
$C_{initial(1,5-DHN)}$ represents concentration of 1,5-DHN

### 2.5. Photocatalytic E-Z Isomerization of Stilbene

The reaction was conducted with 0.2 mmol of *trans*-stilbene (36 mg), 15 mg photocatalyst, in 2 mL DMF at room temperature
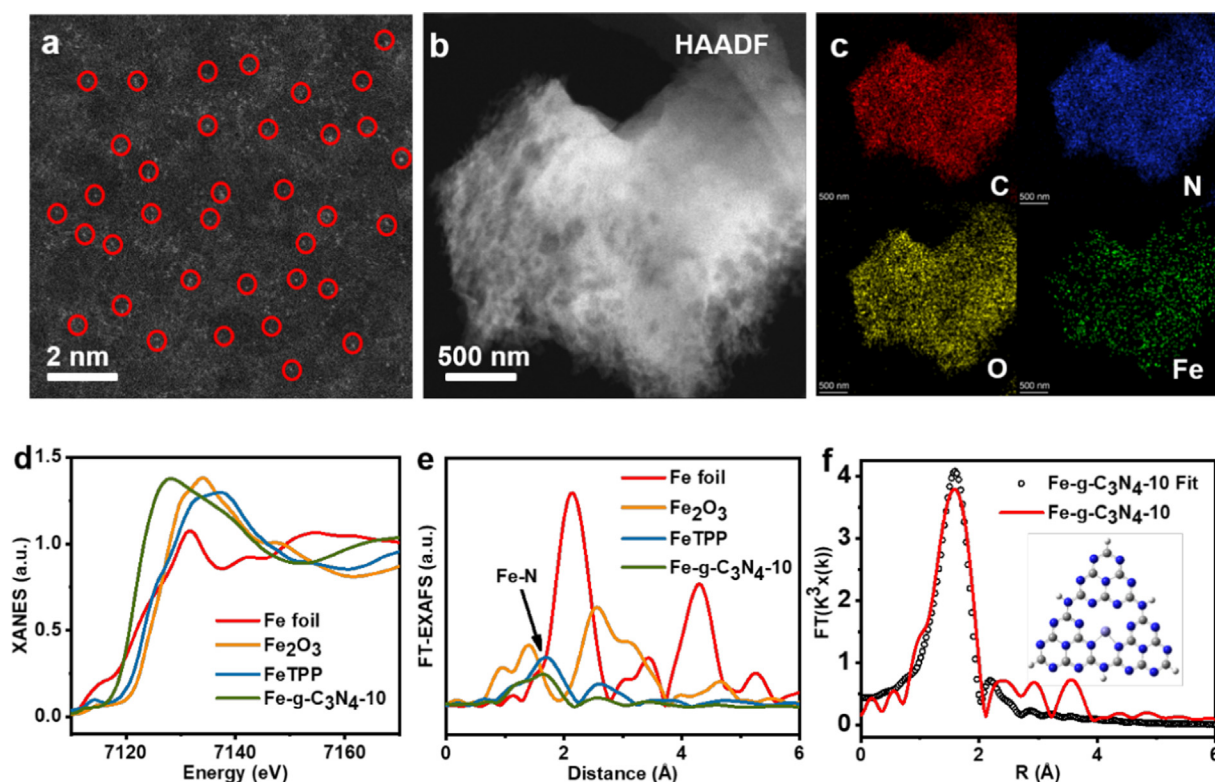


**Fig. 1.** (a) AC-HAADF-STEM image of Fe-g-$C_3N_4$-10. The bright dots marked with the red circle indicate the single atom. (b-c) HAADF-STEM image as well as the corresponding EELS mappings of Fe-g-$C_3N_4$-10. (d) K-edge XANES spectra of Fe-g-$C_3N_4$-10, Fe foil, $Fe_2O_3$ and FeTPP. (e) Fourier transforms of the $k^3$-weighted K-edge EXAFS spectra of Fe-g-$C_3N_4$-10, Fe foil, $Fe_2O_3$ and FeTPP. (f) FT-EXAFS curve fitting of Fe-g-$C_3N_4$-10 at R space (The inset is Fe-g-$C_3N_4$-10 model optimized by DFT theory calculation). (For interpretation of the references to colour in this figure legend, the reader is referred to the web version of this article.)
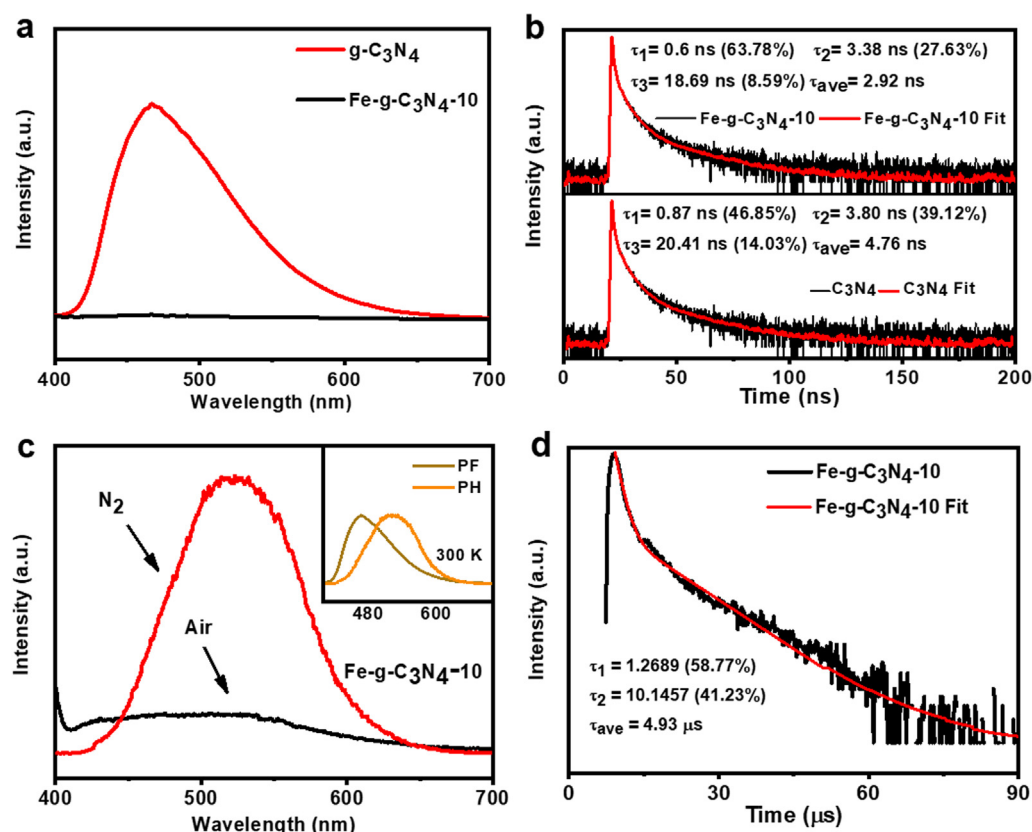
**Fig. 2.** (a) The PF spectra and (b) Time-resolved PF kinetics ($\lambda_{ex}$ = 375 nm). (c) The PH spectra of Fe-g-$C_3N_4$-10 in $N_2$ and Air. The inset is its normalized steady-state PF and PH spectra. (d) Time-resolved PH kinetics ($\lambda_{ex}$ = 375 nm).

under white LED radiation (20 W, 100 W·m$^{-2}$) for 48 h. 1,3,5-Trimethylbenzene as an internal standard substance based on $^1$H NMR analysis.

## 3. Results and discussion

### 3.1. Characterization of Fe-g-$C_3N_4$

Metal ions, such as FeCl$_3$, can chelate with N atom of dicyandiamide forming metal coordination complex, which provide excellent precursor for the fabrication of single-atom Fe-N$_x$ sites. Through one-step pyrolysis, the Fe doped graphitic carbon nitride was prepared with various ratios of FeCl$_3$ and dicyandiamide, denoted as Fe-g-$C_3N_4$-M (M = 1, 5, 10, 15, 20, represent the mass ratio of FeCl$_3$). None metal doped graphitic carbon nitride (g-$C_3N_4$) was also prepared for comparison. Among these samples, Fe-g-$C_3N_4$-10 shows the best photocatalytic performance, which were studied in detail.

The scanning electron microscope (SEM) of Fe doped graphitic carbon nitride show block-like structures stacked by lamellar, similar to that of g-$C_3N_4$ (Fig.S1 and S2). As increasing the Fe amount, the UV–vis absorption edge of these Fe doped g-$C_3N_4$ show significant red shift, which improves the absorption ability of visible light (Fig.S3). For Fe-g-$C_3N_4$-10, the Fe content is 2.95 wt% detected by the Inductively coupled plasma optical emission spectrometry (ICP-OES) (Table S1). The pore size of Fe-g-$C_3N_4$-10 is mainly distributed around 30 nm, and its surface area slightly reduce to 3.69 m$^2$·g$^{-1}$ when compared with g-$C_3N_4$ (Fig.S4). The individual Fe sites appeared as high-density bright dots in the aberration-corrected high-angle annular dark-field scanning transmission electron microscopy (AC-HAADF-STEM) image (Fig. 1a), and there are no Fe nanoclusters or nanoparticles are observed (Fig.S5), indi-

cating that the single-site dispersion of Fe atoms on the carbon support. In addition, the electron energy loss spectroscopy (EELS) elemental mapping reveals that C, N, O and Fe are uniform distributed (Fig. 1b and 1c). As the iron ratio increases to 15%, there are shadows appearing in HRTEM of Fe-g-$C_3N_4$-15, and the lattice fringe spacing of 0.204 nm corresponds to the 110 crystal plane of the Fe nanocluster (Fe$^0$) (Fig.S6), indicating that more Fe ratio results in the Fe$^0$ species formation.

In the powder X-ray diffraction (XRD) of the Fe-g-$C_3N_4$, the peak at 27.5° can be attributed to 002 crystal planes of g-$C_3N_4$, and there is little shift at this position as increasing the Fe mass ratio to 20% (Fig.S7). It means that the interlayer distance doesn't change. In other words, Fe dopants may be located in the six-fold of g-$C_3N_4$ rather than the interlayer space [31,32]. The peak observed at 13.1° indexed as the 100 plane corresponds to the in-plane structural packing motif of tristriazine units. X-ray photoelectron spectroscopy (XPS) was carried out to further reveal the chemical composition and states of Fe dopants. For the XPS spectra of N 1s from g-$C_3N_4$, it can be decomposed into four peaks, those are located at 398.5 eV, 399.8 eV, 401.2 eV and 404.3 eV. They can be ascribed to N atoms of C − N = C, tertiary nitrogen N − C$_3$, C-N − H groups, and π-excitations from low to high energy, respectively [33–35]. As shown in Fig.S9, all these peaks show positive shift after doping with Fe, especially for the N atoms of C-N = C with larger positive shift (0.3 eV), similar results can also be observed for the C 1s. It further indicates that Fe dopant is in the six-fold cavity containing C and N atoms, and coordinate with the N atoms of C-N = C (pyridine N).

The X-ray absorption spectroscopy at Fe K-edge was performed to further determine the valance states and coordination environment of Fe species on the atomic scale. Fig. 1d shows the Fe K-edge X-ray absorption near-structure (XANES) of Fe-g-$C_3N_4$-10, Fe foil,
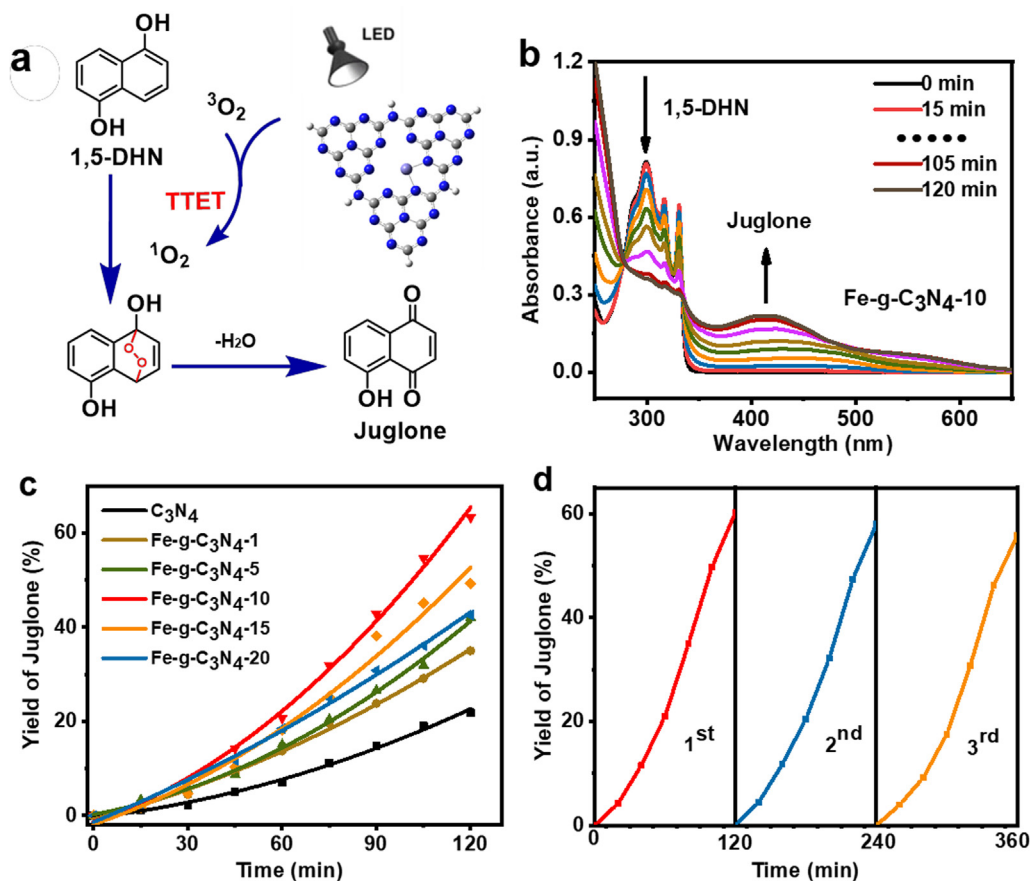
**Fig. 3.** (a) Reaction mechanism diagram for photooxidation of 1,5-DHN. (b) UV - vis absorption spectral changes for photooxidation of 1,5-DHN ($1.0 \times 10^{-2}$ M) in acetonitrile/water = 5/1 (v/v), m (Fe-g-$C_3N_4$-10) = 15 mg. (c) Changes in the yield of juglone from 1,5-DHN catalyzed by Fe-g-$C_3N_4$-M over time. (d) Stability of Fe-g-$C_3N_4$-10 photooxidation of 1,5-DHN.

$Fe_2O_3$ and FeTPP. The XANES spectrum of Fe-g-$C_3N_4$-10 is between Fe foil and FeTPP, indicating the existence of the Fe oxidized state (Fe$^{\delta+}$, $0 < \delta < 2$). Only a peak around 1.6 Å is observed, but no peaks are around 2.1 Å associated with the Fe-Fe and 2.6 Å associated with the Fe-O in the $k^3$-weighted Fourier transforms of Fe K-edge from extended X-ray absorption fine structure (FT-EXAFS) (Fig.1e). The similarity further suggests the atomic dispersion of Fe sites in the Fe-g-$C_3N_4$-10 without Fe$^0$ species. The scattering peak around 1.6 Å is very similar to FeTPP containing Fe-$N_4$, which shows that Fe is primarily coordinated with 4 N atoms. The corresponding fitted R-space curve in Fig. 1f further shows that the coordination number of the Fe species within the Fe-g-$C_3N_4$-10 is 4.1 and the bond length is 2.11 Å. The detailed fitting parameters of the Fe-g-$C_3N_4$-10 and the reference sample (Fe foil) can be found in Table S2. According to the above results, the g-$C_3N_4$, FeTPP and Fe-g-$C_3N_4$-10 molecular models are optimized using density functional theory (DFT) calculations, and isolated Fe atom can coordinate with the N atoms and stably exist in the six-fold cavity of g-$C_3N_4$ (Fig. 1f and Fig.S13).

The photoluminescence of g-$C_3N_4$ and Fe-g-$C_3N_4$-10 were tested, including steady-state and time-resolved prompt fluorescence (PF) and phosphorescence (PH). g-$C_3N_4$ has a fluorescent peak at 460 nm, which is caused by the $\pi$-$\pi^*$ transition in g-$C_3N_4$ [36]. But the incorporation of Fe greatly quenches the PF intensity of the fluorescence emission (Fig. 2a). The average PF lifetime of g-$C_3N_4$ is 4.76 ns, while that of Fe-g-$C_3N_4$ is only 2.92 ns (Fig. 2b). The roughly decrease of the average PF lifetime may relate to the acceleration of the nonradiative ISC process in Fe-g-$C_3N_4$-10. For the emission of Fe-g-$C_3N_4$-10 at 525 nm (Fig. 2c, the inset shows the

normalized PF and PH emission spectra), it is sensitive to $O_2$, and its lifetime prolongs to 4.93 μs (Fig. 2c and 2d). It indicates that this emission can be attributed to PH. PH generally exhibits a much longer lifetime than PF. The observation of pH clearly suggests the existence of triplet excitons in this system. The above discussions reveal that single atom Fe-$N_4$ site in Fe-g-$C_3N_4$-10 can enhance triplet exciton generation.

### 3.2. Photocatalytic oxidation of 1,5-DHN and its mechanism

Although molecular oxygen ($O_2$) is a green and abundant oxidant, it hardly oxidizes most organics under mild conditions due to the spin forbidden [37]. Through triplet energy transfer to sensitize $O_2$ into $^1O_2$, it is a green way to photocatalytic oxidation of 1,5-DHN for the preparation of juglone with hemostatic and antibacterial activities. Therefore, it was selected as the model reaction to evaluate the triplet-energy transfer performance of the Fe-g-$C_3N_4$ under visible light illumination. With the assistant of light and photocatalysts, the intensity of the absorption peak of 1,5-DHN at 300 nm continues to decrease, while the intensity of the absorption peak at 425 nm attributed to product juglone increases as prolonging the irradiation time (Fig. 3a-3b). For g-$C_3N_4$ as the photocatalyst, its yield of juglone was only 22% after 2 h' reaction (Fig.S14a). As increasing the Fe mass ratio to 10%, the yield of juglone increases to 63% (Fig. 3b and Table S3), which is the best one among these photocatalysts (Fig. 3c and Fig.S14b-e). After three cycles of reaction, there is no obvious loss in the photocatalysis performance for Fe-g-$C_3N_4$-10 (Fig. 3d).
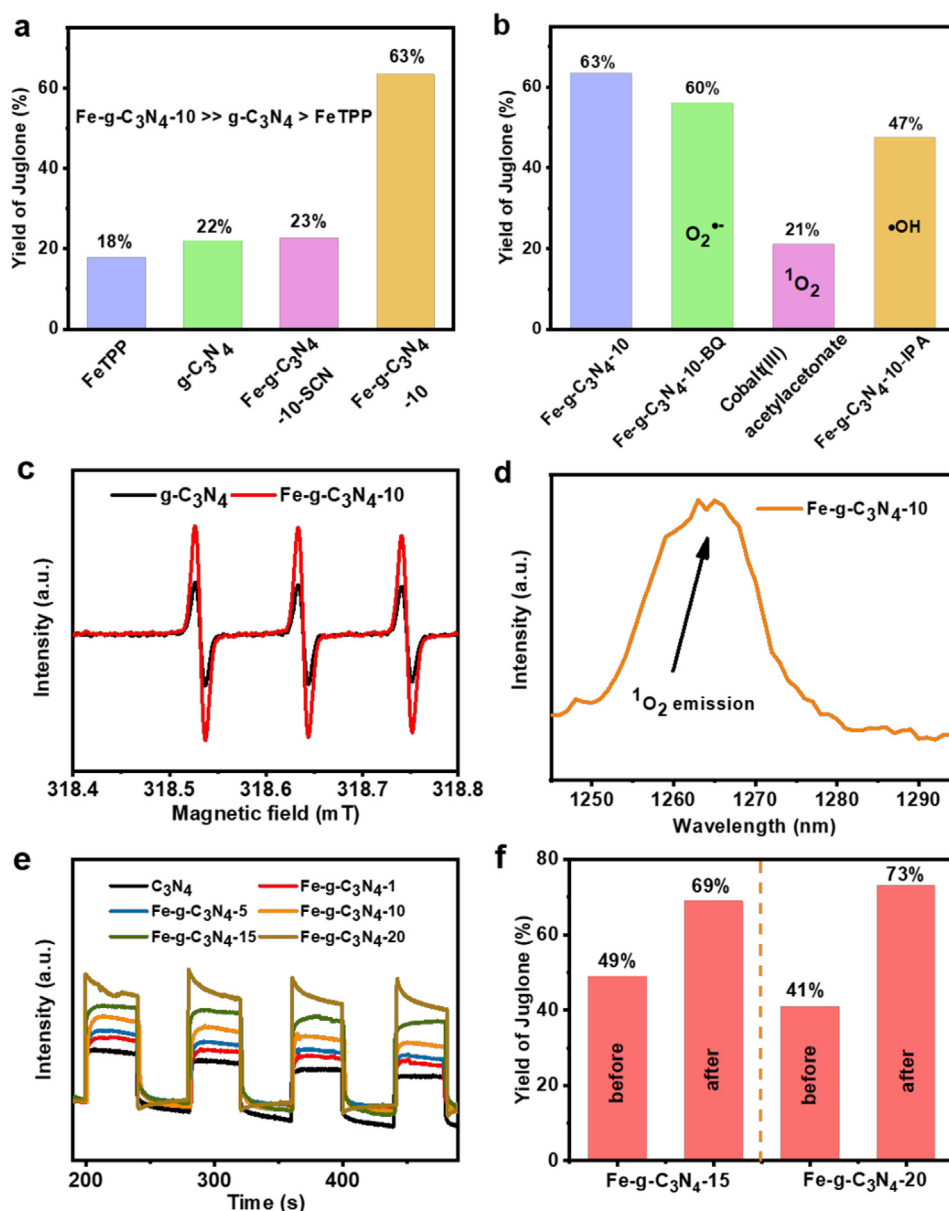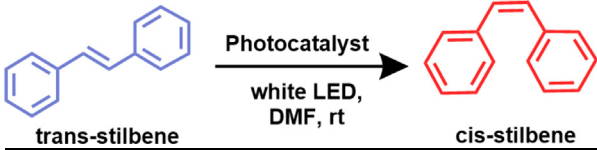
**Fig. 4.** (a) Yield of juglone for different photocatalysts. (b) Yield of juglone for Fe-g-C$_3$N$_4$-10 in the presence of different quenchers. (c) ESR spectra of g-C$_3$N$_4$ and Fe-g-C$_3$N$_4$-10 upon irradiation in the presence of TEMP. (d) $^1$O$_2$ emission signal of Fe-g-C$_3$N$_4$-10 under 532 nm excitation. (e) Transient photocurrent response curve (λ > 420 nm light irradiation). (f) Yield of juglone before and after acid pickling for Fe-g-C$_3$N$_4$-15 and Fe-g-C$_3$N$_4$-20.

Potassium thiocyanide (KSCN) poisoning experiment was performed to verify the active site, wherein SCN$^{-1}$ as the molecule probe can coordinate with transition metals and interrupt the adsorption of O$_2$ to metal [38,39]. After the addition of KSCN, the yield of juglone decreases from 63% to 23%, close to that of g-C$_3$N$_4$ (Fig. 4a and S14f). FeTPP containing Fe-N$_4$ structure can be considered as the Fe-N$_4$ model molecular. The yield of juglone catalyzed by FeTPP with the same surface Fe content was only 18% (Fig. 4a). Interestingly, the yield of juglone catalyzed by Fe-g-C$_3$N$_4$-10 (63%) is higher than the sum of FeTPP (18%) and g-C$_3$N$_4$ (22%). It indicates that Fe-N$_4$ rather than Fe$^0$ species is active site and there is a significant synergistic effect between Fe-N$_4$ and g-C$_3$N$_4$ in Fe-g-C$_3$N$_4$-10.

O$_2$ can be transformed into highly active oxygen species (ROS), such as superoxide radicals (O$_2^-$), hydroxyl radicals ( OH), singlet oxygen($^1$O$_2$) or hydrogen peroxide(H$_2$O$_2$) [40]. OH and O$_2^-$ are generated through electron transfer process that competes with the energy transfer process related to $^1$O$_2$ generation. In order to determine the ROS in photooxidation of 1,5-DHN, cobalt (III) acety-

lacetonate, benzoquinone (BQ) and isopropanol (IPA) were selected as the quenchers to capture $^1$O$_2$, O$_2^-$ and OH respectively. When cobalt acetylacetonate added, the yield of juglone was significantly reduced (Fig. 4b), indicating that $^1$O$_2$ is the main ROS in this photocatalytic reaction. The $^1$O$_2$ generation is verified by electron spin resonance (ESR) test and $^1$O$_2$ emission. 2,2,6,6-tetramethylpiperidine (TEMP) can act as selective capture agent for $^1$O$_2$, which can be selectively oxidized by $^1$O$_2$ to generate 2,2,6,6-tetramethylpiperidine nitrogen oxide (TEMPO) and detected by ESR [41]. The characteristic triplet signal (intensity ratio of 1:1:1, g = 2.002). Without light, there are no signals for Fe-g-C$_3$N$_4$-10 (Fig. S16). As increasing the irradiation time, characteristic peak signals of TEMPO increases, and the signal of Fe-g-C$_3$N$_4$-10 is higher than that of g-C$_3$N$_4$ (Fig. 4c). The characteristic fluorescent emission of $^1$O$_2$ can also be observed at 1265 nm (Fig. 4d), further confirming the existence of $^1$O$_2$. Compared with Figure S17, only $^1$O$_2$ observed instead of O$_2^-$ for Fe-g-C$_3$N$_4$-10 further indicates that the promotion of energy transfer.

**Table 1**

Reaction Conditions catalyzed by different samples and the yield of *cis*-stilbene



trans-stilbene → Photocatalyst, white LED, DMF, rt → cis-stilbene

| entry | photocatalyst | Photocatalyst amount (mg) | temperature | yield (%) |
|---|---|---|---|---|
| 1 | g-C$_3$N$_4$ | 15 mg | rt | 3% |
| 2 | Fe-g-C$_3$N$_4$-1 | | rt | 9% |
| 3 | Fe-g-C$_3$N$_4$-5 | | rt | 24% |
| 4 | Fe-g-C$_3$N$_4$-10 | | rt | 44% |
| 5 | Fe-g-C$_3$N$_4$-15 | | rt | 30% |
| 6 | Fe-g-C$_3$N$_4$-20 | | rt | 20% |
| 7 | Fe-g-C$_3$N$_4$-15-H | | rt | 51% |
| 8 | Fe-g-C$_3$N$_4$-20-H | | rt | 60% |
| 9[a] | Fe-g-C$_3$N$_4$-10 | | rt | trace |
| 10[b] | Fe-g-C$_3$N$_4$-10 | | 60℃ | trace |
| 11[c] | – | 0 | rt | trace |

[a] Excitation in the dark in the presence of Fe-g-C$_3$N$_4$-10; [b] Further investigate the effect of reaction temperature; [c] Excitation under white LED in the absence of photocatalysts.

For Fe-g-C$_3$N$_4$-15 and Fe-g-C$_3$N$_4$-20, further increasing Fe ratio to 15% and 20% results in the juglone yield decreasing to 49% and 41% respectively (Fig.S14d-e, Table S3). Associated with the structure difference between these photocatalysts, the higher transient photocurrent response may be due to the formation of Fe$^0$ species based on the excessive Fe loading (Fig.S6). Unlike conventional results, the higher transient photocurrent response, the lower photocatalysis performance (Fig. 4e). It indicates that $^1O_2$ mainly sprang from the energy transfer rather than the electron transfer from the holes oxidation for the O$_2$$^{·-}$ [42]. The Fe$^0$ are removed by acid pickling (Fig.S20), only leaving Fe-N$_4$ sites. It interesting that the photocatalysis performance of Fe-g-C$_3$N$_4$-15 and Fe-g-C$_3$N$_4$-20 increase to 69% and 73% after acid pickling respectively (Fig. 4f and Table S3). It is higher than that of Fe-g-C$_3$N$_4$-10 (63%), resulting from the more Fe-N$_4$ active sites in the photocatalyst. The results of ICP-OES further confirmed the content of Fe-N$_4$ active sites in Fe-g-C$_3$N$_4$-15 and Fe-g-C$_3$N$_4$-20 are significantly higher than that of Fe-g-C$_3$N$_4$-10 (Table S4). Electron transfer always complete with electron transfer [43,44]. Therefore, Fe-N$_4$ can promote the triplet energy transfer, but Fe$^0$ promotes the electron transfer meanwhile suppresses the energy transfer process.

### 3.3. Photocatalytic E-Z Isomerization of Stilbene

The maximum phosphorescence emission of Fe-g-C$_3$N$_4$-10 is located at 520 nm, indicating that its triplet energy level is close to the energy level of E-Z Isomerization of stilbene. After visible light irradiation, the photocatalyst can transfer the triplet energy to *trans*-stilbene to generate *cis*-stilbene (Table 1), which is confirmed by $^1$H NMR (Fig.S21). For the pure g-C$_3$N$_4$, the yield of the *cis*-stilbene is only 3%. After introducing Fe-N$_4$ active sites, the yield increases to 44% for Fe-g-C$_3$N$_4$-10. Further increasing the amount of Fe, the yield decreases to 20% for Fe-g-C$_3$N$_4$-20. But after pickling, the maximum yield photocatalyzed by Fe-g-C$_3$N$_4$-20-H comes to 60%. Compared their Fe species, Fe-g-C$_3$N$_4$-20-H with more Fe-N active sites can promote the triplet energy transfer for photocatalytic E-Z Isomerization of stilbene. But Fe-g-C$_3$N$_4$-20 processing the excessive Fe$^0$ content promotes electron transfer and inhibits the triplet energy transfer process, resulting in the yield decrease, which is similar to that of $^1O_2$ photosensitization. These results indicate that the optimized catalyst can process higher triplet energy level for photocatalysis.

### 4. Conclusion

In summary, we have developed a robust method for the fabrication of metal-nitrogen single atom sites in heterogeneous photocatalyst of g-C$_3$N$_4$, which prolongs its triplet lifetime to 4.93 μs and can efficiently promote its triplet energy transfer process. Benefiting from it, the yield of the photooxidation of 1,5-DHN to juglone comes to 63%, which is 3 times higher than that of g-C$_3$N$_4$. The yield of *cis*-stilbene is up to 60% catalyzed by Fe-g-C$_3$N$_4$-20-H with the highest Fe-N$_4$ content. Associated with the structure analysis of photocatalyst, Fe-N$_4$ in carbon nitride can promote its triplet energy transfer while Fe$^0$ can inhibit it because of it promotes the competitive electron transfer process. This work is conductive to the development of heterogeneous triplet-state photocatalysts in the light-to-energy conversion applications.

### Declaration of Competing Interest

The authors declare that they have no known competing financial interests or personal relationships that could have appeared to influence the work reported in this paper.

### Appendix A. Supplementary data

Supplementary data to this article can be found online at https://doi.org/10.1016/j.jcat.2021.09.010.

### References

[1] B. Wu, L. Zhang, B. Jiang, Q.i. Li, C. Tian, Y. Xie, W. Li, H. Fu, Ultrathin Porous Carbon Nitride Bundles with an Adjustable Energy Band Structure toward Simultaneous Solar Photocatalytic Water Splitting and Selective Phenylcarbinol Oxidation, Angew. Chem. Int. Ed. 60 (9) (2021) 4815–4822.

[2] Y. Zhu, C. Lv, Z. Yin, J. Ren, X. Yang, C.-L. Dong, H. Liu, R. Cai, Y.-C. Huang, W. Theis, S. Shen, D. Yang, A [001]-Oriented Hittorf's Phosphorus Nanorods/

Polymeric Carbon Nitride Heterostructure for Boosting Wide-Spectrum-Responsive Photocatalytic Hydrogen Evolution from Pure Water, Angew. Chem. Int. Ed. 59 (2) (2020) 868–873.

[3] M.S. Zhu, S. Kim, L. Mao, M. Fujitsuka, J.Y. Zhang, X.C. Wang, M. Fujitsuka, Metal-Free Photocatalyst for H₂ Evolution in Visible to Near-Infrared Region: Black Phosphorus/Graphitic Carbon Nitride, J. Am. Chem. Soc. 139 (2017) 13234–13242.

[4] H.J. Yu, R. Shi, Y.X. Zhao, T. Bian, Y.F. Zhao, C. Zhou, G.I.N. Waterhouse, L.-Z. Wu, C.-H. Tung, T.R. Zhang, Alkali-Assisted Synthesis of Nitrogen Deficient Graphitic Carbon Nitride with Tunable Band Structures for Efficient Visible-Light-Driven Hydrogen Evolution, Adv. Mater. 29 (2017) 1605148.

[5] L. Lin, Z. Lin, J. Zhang, X.u. Cai, W. Lin, Z. Yu, X. Wang, Molecular-level insights on the reactive facet of carbon nitride single crystals photocatalysing overall water splitting, Nat. Catal. 3 (8) (2020) 649–655.

[6] L.N. Zhao, Z.L. Zhao, Y.X. Li, X.Y. Chu, Z.J. Li, Y. Qu, L.L. Bai, L.Q. Jing, The synthesis of interface-modulated ultrathin Ni(II) MOF/g-C₃N₄ heterojunctions as efficient photocatalysts for CO₂ reduction, Nanoscale 12 (2020) 10010–10018.

[7] J. Wang, S.W. Cao, J.G. Yu, Nanocages of Polymeric Carbon Nitride from Low-Temperature Supramolecular Preorganization for Photocatalytic CO₂ Reduction, Sol. RRL. 4 (2020) 1900469.

[8] A. Savateev, I. Ghosh, B. König, M. Antonietti, Photoredox Catalytic Organic Transformations using Heterogeneous Carbon Nitrides, Angew. Chem. Int. Ed. 57 (49) (2018) 15936–15947.

[9] W.-J. Ong, L.-L. Tan, Y.H. Ng, S.-T. Yong, S.-P. Chai, Graphitic Carbon Nitride (g-C₃N₄)-Based Photocatalysts for Artificial Photosynthesis and Environmental Remediation: Are We a Step Closer To Achieving Sustainability?, Chem Rev. 116 (12) (2016) 7159–7329.

[10] Q. Liu, L.-Z. Wu, Recent advances in visible-light-driven organic reactions, Nat. Sci. Rev. 4 (2017) 359-380.

[11] I. Ghosh, J. Khamrai, A. Savateev, N. Shlapakov, M. Antonietti, B. König, Organic semiconductor photocatalyst can bifunctionalize arenes and heteroarenes, Science 365 (6451) (2019) 360–366.

[12] A. Savateev, I. Ghosh, B. König, M. Antonietti, Photoredoxkatalytische organische Umwandlungen an heterogenen Kohlenstoffnitriden, Angew. Chem. 130 (49) (2018) 16164–16176.

[13] J. Li, Y. Chen, X. Yang, S. Gao, R. Cao, Visible-light-mediated high-efficiency catalytic oxidation of sulfides with wrinkled C₃N₄ nanosheets, J Catal. 381 (2020) 579–589.

[14] J. Liu, Y. Liu, N. Liu, Y. Han, X. Zhang, H. Huang, Y. Lifshitz, S.-T. Lee, J. Zhong, Z. Kang, Metal-free efficient photocatalyst for stable visible water splitting via a two-electron pathway, Science 347 (6225) (2015) 970–974.

[15] C.F. Huang, Y.P. Wen, J. Ma, D.D. Dong, Y.F. Shen, S.Q. Liu, H.B. Ma, Y.J. Zhang, Unraveling fundamental active units in carbon nitride for photocatalytic oxidation reactions, Nat. Commun. 12 (2021) 320.

[16] H.L. Wang, L.S. Zhang, Z.G. Chen, J.Q. Hu, S.J. Li, Z.H. Wang, J.S. Liu, X.C. Wang, Semiconductor heterojunction photocatalysts: design, construction, and photocatalytic performances, Chem. Soc. Rev. 43 (2014) 5234–5244.

[17] Y.-J. Yuan, Z.-T. Yu, D.-Q. Chen, Z.-G. Zou, Metal-complex chromophores for solar hydrogen generation, Chem. Soc. Rev. 46 (3) (2017) 603–631.

[18] N.J. Turro, V. Ramamurthy, J.C. Scaiano, Modern Molecular Photochemistry of Organic Molecules, Photochem. Photobiol. 88 (2012).

[19] J.Z. Zhao, W.H. Wu, J.F. Sun, S. Guo, Triplet photosensitizers: from molecular design to applications, Chem. Soc. Rev. 42 (2013) 5323–5351.

[20] W. Zhao, Z. He, B.Z. Tang, Room-temperature phosphorescence from organic aggregates, Nat. Rev. Mater. 5 (12) (2020) 869–885.

[21] Y. Qian, D. Li, Y. Han, H.-L. Jiang, Photocatalytic Molecular Oxygen Activation by Regulating Excitonic Effects in Covalent Organic Frameworks, J. Am. Chem. Soc. 142 (49) (2020) 20763–20771.

[22] A.Q. Ma, H.Q. Chen, Y.H. Cui, Z.Y. Luo, R.J. Liang, Z.H. Wu, Z. Chen, T. Yin, J. Ni, M. B. Zheng, L.T. Cai, Metalloporphyrin Complex-Based Nanosonosensitizers for Deep-Tissue Tumor Theranostics by Noninvasive Sonodynamic Therapy, Small 15 (2019) 1804028.

[23] W. Wu, C. Han, Q. Zhang, Q. Zhang, Z. Li, D.J. Gosztola, G.P. Wiederrecht, M. Wu, Functionalizing carbon nitride with heavy atom-free spin converters for enhanced ¹O₂ generation, J. Catal. 361 (2018) 222–229.

[24] S. Xue, T. Zhang, X. Wang, Q. Zhang, S. Huang, L. Zhang, L. Zhang, W. Zhu, Y. Wang, M. Wu, Q. Zhao, P. Li, W. Wu, Cu, Zn Dopants Boost Electron Transfer of

[25] Carbon Dots for Antioxidation, Small 17 (31) (2021) 2102178, https://doi.org/10.1002/smll.v17.3110.1002/smll.202102178.

[26] X.Y. Lu, S.S. Gao, H. Lin, J.L. Shi, Single-Atom Catalysts for Nanocatalytic Tumor Therapy, Small 17 (2021) 2004467.

[27] Q. Wang, T. Ina, W.-T. Chen, L. Shang, F.F. Sun, S.H. Wei, D.X. Sun-Waterhouse, S.G. Telfer, T.R. Zhang, G.I.N. Waterhouse, Evolution of Zn(II) single atom catalyst sites during the pyrolysis-induced transformation of ZIF-8 to N-doped carbons, Sci. Bull. 65 (2020) 1743–1751.

[28] E. Vorobyeva, V.C. Gerken, S. Mitchell, et al., Activation of Copper Species on Carbon Nitride for Enhanced Activity in the Arylation of Amines, ACS Catal. 10 (2020) 11069–11080.

[29] Y.S. Wang, T. Yang, Q.J. He, Strategies for engineering advanced nanomedicines for gas therapy of cancer, Nat. Sci. Rev. 7 (2020) 1485-1512.

[30] H. Wang, S. Jiang, W. Shao, X. Zhang, S. Chen, X. Sun, Q. Zhang, Y.i. Luo, Y.i. Xie, Optically Switchable Photocatalysis in Ultrathin Black Phosphorus Nanosheets, J. Am. Chem. Soc. 140 (9) (2018) 3474–3480.

[31] W. Wu, D. Mao, S. Xu, Kenry, F. Hu, X. Li, D. Kong, B. Liu, Polymerization-Enhanced Photosensitization, Chem 4 (8) (2018) 1937–1951.

[32] S. An, G. Zhang, T. Wang, W. Zhang, K. Li, C. Song, J.T. Miller, S. Miao, J. Wang, X. Guo, High-Density Ultra-small Clusters and Single-Atom Fe Sites Embedded in Graphitic Carbon Nitride (g-C₃N₄) for Highly Efficient Catalytic Advanced Oxidation Processes, ACS Nano 12 (9) (2018) 9441–9450.

[33] Z. Chen, S. Pronkin, T.-P. Fellinger, K. Kailasam, G. Vilé, D. Albani, F. Krumeich, R. Leary, J. Barnard, J.M. Thomas, J. Pérez-Ramírez, M. Antonietti, D. Dontsova, Merging Single-Atom-Dispersed Silver and Carbon Nitride to a Joint Electronic System via Copolymerization with Silver Tricyanomethanide, ACS Nano 10 (3) (2016) 3166–3175.

[33] S. Cao, J. Low, J. Yu, M. Jaroniec, Polymeric photocatalysts based on graphitic carbon nitride, Adv. Mater. 27 (13) (2015) 2150–2176.

[34] W. Jiang, W. Luo, J. Wang, M.o. Zhang, Y. Zhu, Enhancement of catalytic activity and oxidative ability for graphitic carbon nitride, J. Photochem. Photobiol. C 28 (2016) 87–115.

[35] J. Wu, J. Chen, Y. Huang, K. Feng, J. Deng, W. Huang, Y. Wu, J. Zhong, Y. Li, Cobalt atoms dispersed on hierarchical carbon nitride support as the cathode electrocatalyst for high-performance lithium-polysulfide batteries, Sci. Bull. 64 (24) (2019) 1875–1880.

[36] Z.B. Zhou, X.H. Niu, L. Ma, J.L. Wang, Revealing the pH-Dependent Photoluminescence Mechanism of Graphitic C₃N₄ Quantum Dots, Adv. Theory Simul. 2 (2019) 1900074.

[37] W. Nam, Y.M. Lee, S. Fukuzumi, Hydrogen Atom Transfer Reactions of Mononuclear Nonheme Metal-Oxygen Intermediates, Acc. Chem. Res. 51 (2018) 2014–2022.

[38] W. Wu, Q. Zhang, X. Wang, C. Han, X. Shao, Y. Wang, J. Liu, Z. Li, X. Lu, M. Wu, Enhancing Selective Photooxidation through Co-Nx-doped Carbon Materials as Singlet Oxygen Photosensitizers, ACS Catal. 7 (10) (2017) 7267–7273.

[39] Y. Xing, Z. Yao, W. Li, W. Wu, X. Lu, J. Tian, Z. Li, H. Hu, M. Wu, Fe/Fe₃C Boosts H₂O₂ Utilization for Methane Conversion Overwhelming O₂ Generation, Angew. Chem. Int. Ed. 60 (16) (2021) 8889–8895.

[40] Y. Zheng, Z.H. Yu, H.H. Ou, A.M. Asiri, Y.L. Chen, X.C. Wang, Black Phosphorus and Polymeric Carbon Nitride Heterostructure for Photoinduced Molecular Oxygen Activation, Adv. Funct. Mater. 28 (2018) 1705407.

[41] S. Wang, L.u. Shang, L. Li, Y. Yu, C. Chi, K. Wang, J. Zhang, R. Shi, H. Shen, G.I.N. Waterhouse, S. Liu, J. Tian, T. Zhang, H. Liu, Metal-Organic-Framework-Derived Mesoporous Carbon Nanospheres Containing Porphyrin-Like Metal Centers for Conformal Phototherapy, Adv. Mater. 28 (38) (2016) 8379–8387.

[42] S. Zhao, X. Zhao, Insights into the role of singlet oxygen in the photocatalytic hydrogen peroxide production over polyoxometalates-derived metal oxides incorporated into graphitic carbon nitride framework, Appl. Catal. B Environ. 250 (2019) 408–418.

[43] X. Wu, W. Wu, X. Cui, J. Zhao, M. Wu, Preparation of Bodipy-ferrocene dyads and modulation of the singlet/triplet excited state of bodipy via electron transfer and triplet energy transfer, J. Mater. Chem. C 4 (14) (2016) 2843–2853.

[44] W. Wu, X. Wu, J. Zhao, M. Wu, Synergetic effect of C^N^N/C^N^N coordination and the arylacetylide ligands on the photophysical properties of cyclometalated platinum complexes, J. Mater. Chem. C 3 (10) (2015) 2291–2301.